Journal of *Marine Science and Engineering*

MDPI

Article

How Does El Niño Affect Predictability Barrier of Its Accompanied Positive Indian Ocean Dipole Event?

Da Liu [1,2], Wansuo Duan [2,3,*] and Rong Feng [2]

[1] National Meteorological Center, Beijing 100081, China; liuda@cma.gov.cn
[2] State Key Laboratory of Numerical Modeling for Atmospheric Sciences and Geophysical Fluid Dynamics (LASG), Institute of Atmospheric Physics, Chinese Academy of Sciences, Beijing 100029, China; fengrong@lasg.iap.ac.cn
[3] College of Marine Science, University of Chinese Academy of Sciences, Beijing 100049, China
* Correspondence: duanws@lasg.iap.ac.cn; Tel.: +86-10-8299-5302; Fax: +86-10-82995172

Abstract: The effects of El Niño on the predictability of positive Indian Ocean dipole (pIOD) events are investigated by using the GFDL CM2p1 coupled model from the perspective of error growth. The results show that, under the influence of El Niño, the summer predictability barrier (SPB) for pIOD tends to intensify and the winter predictability barrier (WPB) is weakened. Since the reason for the weakening of WPB has been explained in a previous study, the present study attempts to explore why the SPB is enhanced. The results demonstrate that the initial sea temperature errors, which are most likely to induce SPB for pIOD with El Niño, possess patterns similar to those for pIOD without El Niño, whose dominant errors concentrate in the tropical Pacific Ocean (PO), with a pattern of negative SST errors occurring in the eastern and central PO and subsurface sea temperature errors being negative in the eastern PO and positive in the western PO. By tracking the development of such initial errors, it is found that the initial errors over PO lead to anomalous westerlies in the southeastern Indian Ocean (IO) through the effect of double-cell Walker circulation. Such westerly anomalies are inhibited by the strongest climatological easterly wind and the southeasterlies related to the pIOD event itself in summer, while they are enhanced by El Niño. This competing effect causes the intensified seasonal variation in latent heat flux, with much less loss in summer under the effect of El Niño. The greater suppression of the loss of latent heat flux favors the positive sea surface temperature (SST) errors developing much faster in the eastern Indian Ocean in summer, and eventually induces an enhanced SPB for pIOD due to El Niño.

Keywords: Pacific Ocean; Indian Ocean; IOD events; El Niño; initial errors; summer predictability barrier

Citation: Liu, D.; Duan, W.; Feng, R. How Does El Niño Affect Predictability Barrier of Its Accompanied Positive Indian Ocean Dipole Event?. *J. Mar. Sci. Eng.* **2021**, *9*, 1169. https://doi.org/10.3390/jmse9111169

Academic Editor: Chun-Ta Lai

Received: 8 September 2021
Accepted: 22 October 2021
Published: 24 October 2021

1. Introduction

The Indian Ocean dipole (IOD) is a dominant interannual variability in the tropical Indian Ocean (IO), which is characterized by a west–east dipole pattern in the sea surface temperature anomalies (SSTAs) [1–3]. IOD is prominent during boreal summer and fall, with its intensity peak around October, and then collapses rapidly in the following winter [1,3]. IOD presents two phases, a positive IOD (pIOD) shows positive SSTAs in the western IO (WIO) and negative SSTAs in the southeastern IO (SEIO) along with anomalous easterlies around the equator [1]; a negative IOD (nIOD) presents a nearly opposite mode to pIOD, with its amplitude being weaker than that of pIOD [1,4]. The intensity of IOD is usually measured by the dipole mode index (DMI), which is defined by the difference in SSTAs between WIO and SEIO [1]. Additionally, the time at which an IOD occurs depends on whether the DMI exceeds 0.5 standard deviations for three consecutive months [5]. IOD has attracted a great deal of attention due to its significant worldwide climate influences; it not only affects surface temperature and precipitation over the coastal regions of IO, but

also modulates the climate in East Asia, North America and Europe [6–12]. Therefore, it is crucial to predict IOD events successfully.

The predictability of IOD has been assessed in several studies [13–17]. Compared to the 5–6-month lead time for the skillful SST prediction of the WIO and 3–4 months for the SEIO, the lead time for the skillful prediction of IOD events is much shorter with only one season, which indicates that predicting IOD events accurately is still difficult [16,18]. Recent studies showed that the prediction errors of IOD events develop fast during boreal winter and summer, which indicates that the prediction skills of IOD decrease rapidly during these two seasons; therefore, the winter predictability barrier (WPB) and summer predictability barrier (SPB) exist in IOD predictions [15,17,19]. The occurrence of WPB and SPB will cause a rapid decline in IOD forecasting skills, so, in order to improve IOD prediction skills, WPB and SPB should be considered. Studies have been performed to investigate WPB and SPB, and the results demonstrate that WPB is mainly induced by the initial errors of IO, while SPB is generated by the initial uncertainties in the Pacific Ocean (PO) [17,19]. This implies that, beyond IO itself, the uncertainty occurring in PO is also an important factor that affects the predictability of IOD. Liu et al. [17] has explored how PO affects the IOD predictability from the aspect of error growth in the absence of El Niño. The results show that the occurrence of SPB is mainly caused by the seasonal changes in latent heat flux, which is related to the wind anomaly generated by the initial errors in PO [17]. Then, what are the effects of PO if the IOD is accompanied by El Niño?

It is well-known that El Niño/Southern Oscillation (ENSO) is the most significant air–ocean coupled phenomenon in PO, which is closely related to IOD events [20,21]. ENSO can affect IOD through the atmospheric Walker circulation [22–24] and the oceanic dynamics [25,26], and the occurrence and magnitude of IOD can also be modulated by ENSO [20,27]. However, how ENSO affects the predictability of IOD remains to be clarified. Some studies pointed out that the occurrence of IOD is easier to predict when ENSO occurs [5,28], and the prediction skills of IOD in statistical models, especially the prediction skills of intensity, can be effectively improved by introducing the ENSO index [29,30]; meanwhile, other studies suggested that the anomalous atmospheric circulation caused by ENSO can induce a spring persistence barrier for SST in WIO and a winter persistence barrier for SST in EIO, which may limit the prediction skills of IOD [15,31]. However, in the present study, we demonstrate that, when considering the influence of El Niño, which is the warm phase of ENSO, the strength of WPB is decreased, while the intensity of SPB is enhanced (the details can be seen in Section 3), which makes it challenging to determine whether the effects of ENSO on IOD predictability are positive or negative. Under such a situation, further investigations are necessary to understand the dynamical mechanisms of how ENSO affects the IOD predictability. Feng et al. [19] explored the reasons that WPB decreases under the effects of El Niño, and demonstrated that the shortwave radiation flux depresses the development of prediction errors during winter when pIOD events occur with El Niño. Thus, the question of why El Niño increases the strength of SPB will be addressed in the present study.

The perfect model predictability experiments are used to address these problems, in which the prediction uncertainties are only generated by initial errors. The rest of this paper is organized as follows. Section 2 describes the detailed information about the model and experimental strategy. Section 3 shows the predictability barriers of IOD events accompanied by El Niño. Section 4 reveals the effects of El Niño on the spatial characteristics of initial errors and corresponding error growth mechanism. Finally, Section 5 includes a summary and discussion.

2. Model and Experimental Strategy

The Geophysical Fluid Dynamics Laboratory Climate Model version 2p1 (GFDL CM2p1) is used in the present study, which presents great simulation capability for IO and PO climatology as well as IOD and ENSO events [32]. The GFDL CM2p1 coupled model has been widely used in the predictability research for both IOD and ENSO [5,17,19],

which indicates that this model is appropriate to explore the effect of ENSO on IOD predictability. The GFDL CM2p1 contains atmosphere, ocean, land and sea ice components, which are coupled through the GFDL's Flexible Modeling System (FMS, Available online: https://www.gfdl.noaa.gov/~fms, accessed on 1 October 2021). As the oceanic and atmospheric outputs are only applied in this study, we only briefly introduce here the ocean and atmosphere components. The Modular Ocean Model version 4 (MOM4p1) is employed as the ocean component, whose latitudinal resolution is 1°and the meridional resolution is 1° in the middle and high latitudes and reduced to 1/3° around the equator. The vertical levels of MOM4p1 are 50, and the resolution in the upper 225 m is 10 m. The GFDL CM2p1 employs the atmosphere model (AM2p12b) as the atmospheric component, whose horizontal resolution is 2° latitude by 2.5° longitude, with 24 vertical levels. More detailed descriptions and simulation skills regarding the GFDL CM2p1 can be found in Delworth et al. [33] and Groffies [34].

To investigate the influence of El Niño on IOD predictability from the perspective of error growth, perfect model predictability experiments were conducted using the GFDL CM2p1. This means that the GFDM CM2p1 is assumed to be perfect, and the prediction uncertainties of IOD events are only produced by initial errors. The GFDL CM2p1 run for 200 years, with the forcing values being aerosols, land cover, tracer, gases and insolation in 1990. Only in the last 150 years, control runs have been performed to derive the climatological state. The IOD and El Niño events were identified after the elimination of the climatological annual cycle. The average of SSTAs over the region bounded by 5° N to 5° S, and 170° W to 120° W, is defined as the Nino3.4 index, which is used to describe the amplitude of El Niño according to the definition of NOAA in 2005. If the DMI exceeds 0.5 standard deviations for 3 consecutive months and the Nino3.4 is more than 0.5 for 3 months at the same time, we consider that the IOD events occur accompanied by El Niño. As mentioned before, the pIOD events are usually stronger than negative events, and therefore their effects on climate and weather are more significant. Furthermore, in the context of global warming, the frequency and strength of pIOD is increasing obviously [35]. In addition, previous studies showed that when IOD occurred with ENSO events, pIOD was usually accompanied by El Niño [36]. Thus, only pIOD that are accompanied by El Niño are considered in the present study and five such events were selected with different intensities.

Figure 1 shows the DMI of the five selected pIOD events and the Nino3.4 of the accompanying El Niño events, respectively. It is shown that the sign of the Nino3.4 reverses from negative to positive around February, then increases in the following seasons and peaks in December or January in the next year, and declines in the following seasons. The evolution of DMI indicates that pIOD takes place around April, peaks in autumn and weakens rapidly in the following months. These simulations are consistent with prior observations [3,37,38], which confirms that the GFDL CM2p1 is acceptable for studying how El Niño affects pIOD predictability.

The above five pIOD events are regarded as "true states". The dominant period of IOD was considered to be 4 years, which, as shown in [17], is well simulated by the GFDL CM2p1. An IOD event experiences negative to positive phases during 4 years. Thus, the differences in sea temperature between the start month and the months within the 4 preceding years were defined as initial errors, which ensured that the initial errors were plentiful. For each event, the perfect model predictability experiments contained 48 ensemble members at four start months, namely April (−1), July (−1), October (−1) and January (0) ("0" represents the year that IOD attains peak and "−1" is one year before IOD occurs). As the mean lowest depth of the thermocline in the Pacific Ocean is approximately 160–200 m, the initial errors consider the sea temperature component covering the Pacific and Indian oceans (15° N–15° S, 50° E–85° W) from the surface to 225 m. For each initial error, the model will run for 18 months with start month April (−1) and July (−1) and for 12 months with start month October (−1) and January (0).

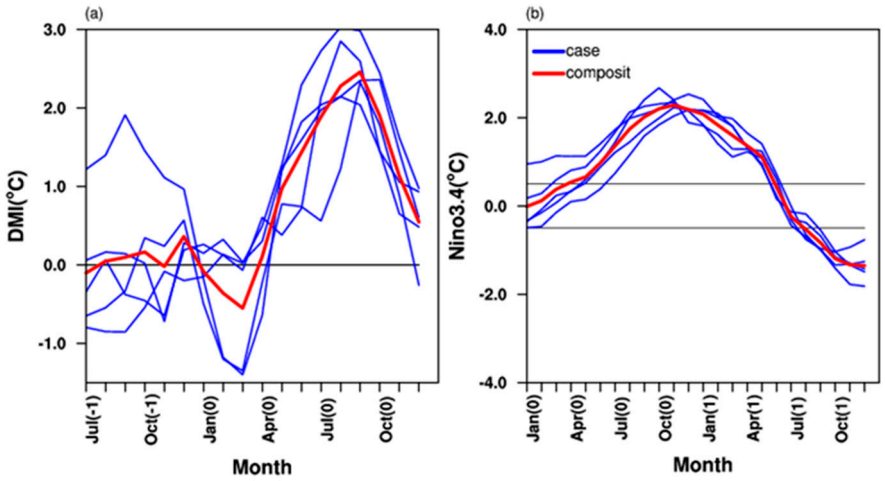

Figure 1. Time series of (**a**) DMI for the five pIOD events that occurred with El Niño from July (−1) to December (0) and that of (**b**) Nino3.4 for the El Niño events from January (0) to December (1) in the GFDL CM2p1. The blue and red curves represent the individual event and their composite mean, respectively.

With these initial errors for the selected pIOD events, 960 predictions were obtained. Based on the predictions and the "true states", the prediction errors are defined by the difference of *DMI* between the predictions and the "true states" as follows:

$$DMI'(t) = |DMI^p(t) - DMI(t)| \quad (1)$$

where the $[DMI]^p$ (t) and DMI (t) are the DMI of the predictions and the referenced pIOD events at leading time t. $[DMI]'$ (t) is the prediction error that is totally induced by the initial errors. The monthly error growth rate is the difference between the [DMI]′ (t) and the later month $[DMI]'$ $(t + 1)$, which implies the changes in prediction errors during one month. To explore the seasonal characteristics of prediction error growth, the sum of the monthly error growth rate for each season is used, and spring is from January to March (JFM), summer is from April to June (AMJ), autumn is from July to September (JAS) and the remainder is winter (OND). Thus, a positive (negative) seasonal error growth rate denotes increasing (decreasing) prediction errors during the season, and a larger absolute value of the seasonal growth rate can indicate faster changes in prediction errors.

3. Predictability Barriers for Positive IOD Events with El Niño

Based on the perfect model experimental strategies, we imposed the predefined initial errors onto the initial states for the chosen five pIOD events accompanied by El Niño; we then run the model with the start months being April (−1) and July (−1) for 18 months and 12 months from the other two start months of October (−1) and January (0) to obtain the predictions. Then, the prediction errors could be calculated. Figure 2 shows the ensemble mean of seasonal error growth rates for predictions of pIOD with El Niño. It is shown that pIOD prediction errors present considerable growth in both AMJ and JAS, while they are reduced in OND. Compared to the results shown in Figure 2 in Liu et al. [17], it is found that the error growth rate of pIOD events with El Niño is much larger in summer than that without El Niño, which reveals that the SPB is enhanced due to the effect of El Niño; meanwhile, decreased error growth occurred in OND, i.e., the WPB was weakened by the El Niño. It should be noticed that the growth rate of pIOD prediction errors is much larger in AMJ, indicating a spring predictability barrier of IOD, which was also shown in [39]. Previous studies demonstrated that when IOD co-occurred with ENSO, wind anomalies associated with ENSO could cause abrupt changes in SST in WIO and intensify the asymmetry of SSTAs in IO during spring (i.e., the AMJ in the present study) by affecting the meridional gradient of sea level pressure, which led to the spring persistence

barrier of IOD and may have been responsible for the fast error growth in spring [40,41]. Regarding additional effects of ENSO on the predictability barrier for IOD, Feng et al. [19], as mentioned in the Introduction, explained the weakened WPB for IOD events; however, the reason that SPB is enhanced by El Niño remains unknown. In the present study, we address this issue.

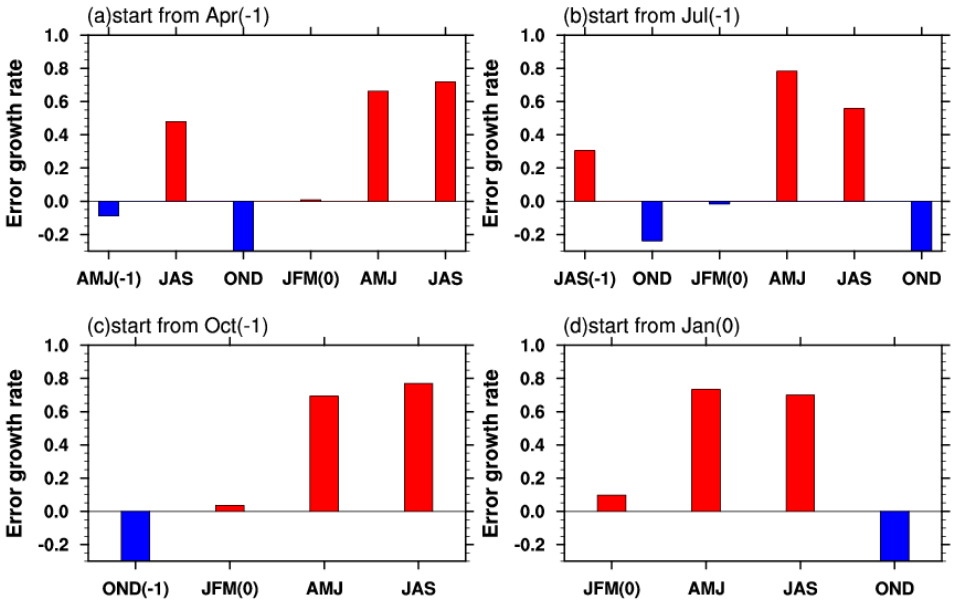

Figure 2. The ensemble mean of seasonal error growth rate for pIOD predictions (histograms) with the start month being: (**a**) April (−1), (**b**) July (−1), (**c**) October (−1) and (**d**) January (0).

4. Reasons for the Enhanced SPB by El Niño

The SPB for IOD predictions has been reported in Liu et al. [17]. They demonstrated that the wind anomalies over SEIO caused by initial errors are greatly suppressed by climatological wind and anomalous wind related to the IOD event itself in summer, which leads to the decreased loss of latent heat flux, eventually bringing about the occurrence of SPB. Moreover, Liu et al. [17] showed that SPB is induced by particular types of initial errors in PO. However, in the present study, we show that the SPB for pIOD events accompanied by El Niño becomes stronger. What is the reason for this?

4.1. Spatial Characteristics of SPB-Related Initial Errors

Since the prediction errors here are only caused by initial errors, the reason that the SPB is enhanced by El Niño needs to be investigated by exploring the differences in the initial errors and their evolutionary mechanisms between the pIOD events accompanied with El Niño and those without El Niño, as presented in Liu et al. [17], which named pure IOD events for convenience. To achieve this, similarly to Liu et al. [17]), we selected the IOD predictions with a significant SPB as the study object, where a significant SPB refers to prediction errors with the seasonal growth rate being the largest in summer. Moreover, to ensure "significance", the differences between the largest and the second largest growth rate were larger than 1.5 standard deviations of the above differences. Thus, a total of 203 predictions were selected, with 62 predictions of the starting month of April (−1), 32 predictions of the starting month of July (−1), 43 predictions of the starting month of October (−1) and the remaining 66 predictions of the starting month of January(0). For the sake of convenience, the initial errors of these 203 predictions were named the SPB-related initial errors.

In the interest of exploring the main features of SPB-related initial errors, we conducted cluster analysis on these initial errors. We divided the 203 SPB-related initial errors into two groups, with 102 initial errors in one group, which is referred to as type-1 errors, and

the remaining 101 initial errors in the other group, which is named type-2 errors. The spatial patterns of the two types of initial errors are composited and plotted in Figure 3. Visibly, the type-1 errors present negative SSTAs in the central PO and larger negative anomalies of subsurface temperature in the eastern PO; meanwhile, in the IO, the surface is covered by negative SST anomalies while the subsurface shows an east–west dipole mode, with the positive temperature anomalies in the eastern IO being much larger. The type-2 initial errors show negative SSTAs over the eastern PO and a dipole pattern of subsurface temperature with negative anomalies in the upper layers of the eastern PO and positive anomalies in the lower layers of the western PO; meanwhile, in the IO, the anomalies are almost opposite to the type-1 initial errors. By observing the evolution of the two types of initial errors starting from any given month (see Figures 4 and 5), we found that they both present a nIOD-like error mode in IO, with positive SSTAs in SEIO and negative SSTAs in WIO in summer; in addition, the SSTAs in PO exhibit a La Niña-like error mode. Such prediction error modes will weaken the strength of predicted pIOD events, even turning them into negative phases of IOD.

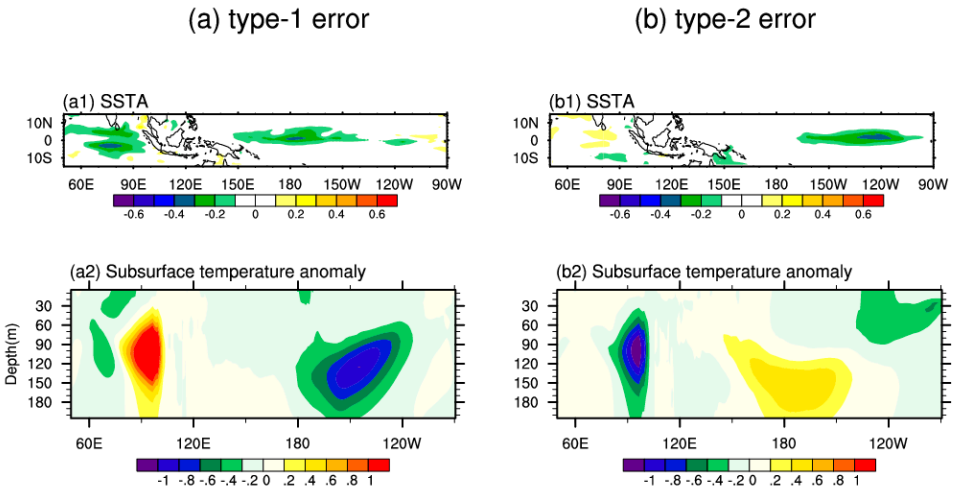

Figure 3. Spatial patterns of the (**a**) type-1 and (**b**) type-2 initial errors that are most likely to induce a significant SPB for pIOD predictions. The upper and lower panels show the surface and the equatorial subsurface component (units: °C, averaged over the region 5° S–5° N).

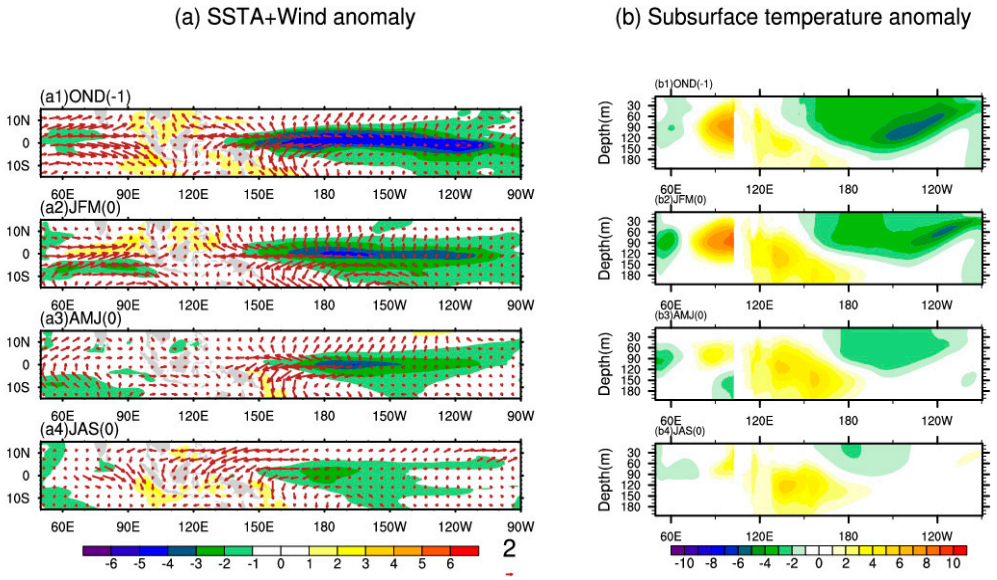

Figure 4. Composite evolutions of (**a**) tropical SST errors (units: °C) and related surface wind anomalies (units: m/s), and (**b**) the equatorial subsurface temperature errors (units: °C; averaged over 5° S by 5° N) induced by the type-1 initial errors with start month being October (−1).

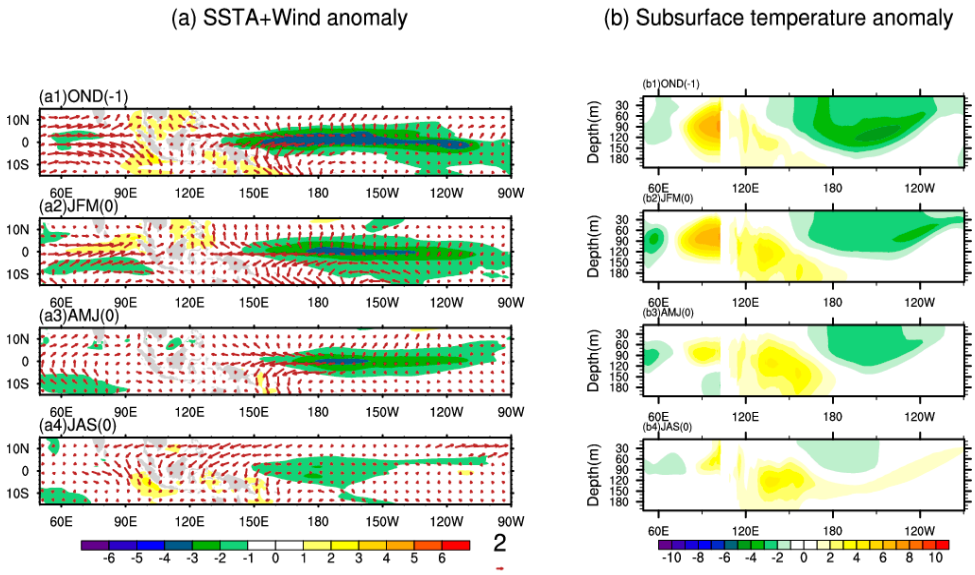

Figure 5. Same as Figure 4, but caused by the type-2 initial errors.

We noticed that the PO components of the two types of initial errors were similar; furthermore, when we observed the evolutions of the two types of initial errors, they also behaved similarly. Specifically, due to the effect of negative SST errors in PO, anomalous easterlies are induced over the PO, which drive the sustainable northwesterly anomalies around the SEIO through the gear effect of double-cell Walker circulation. Such anomalous northwesterlies associated with SPB initial errors are greatly suppressed by climatological southeasterlies and anomalous southeasterlies induced by the pIOD event itself during summer, and then stimulated during the subsequent autumn and winter (Figure 6). Even the anomalous northwesterlies are also depressed in spring; the strength of the climatological and anomalous wind field are both weaker than in summer, which weakens the inhibition of wind anomalies induced by initial errors. Therefore, such seasonal modulation of climatological and IOD-induced wind on the anomalous wind associated with initial errors favors the seasonal variation in latent heat flux, with the maximum positive errors occurring in summer (Figure 7), which is favorable for the fast development of positive SST errors in SEIO and induces SPB for the pIOD events with El Niño.

Combined with the results of the pure IOD events in Liu et al. [17], we found that the SPB for pIOD events is closely related to initial errors in PO for pIOD events with ENSO and pure IOD events, and the SPB-related initial errors share similar spatial characteristics. These SPB-related initial errors, through the effects of double-cell Walker circulation, induce northwesterlies over SEIO, which are significantly decreased by climatological wind and anomalous wind generated by pIOD events in summer. Such suppressed wind anomalies finally stimulate the fast increase in positive SST errors in SEIO by depressing the loss of latent heat flux. However, when comparing the pIOD with and without El Niño, the positive anomalies of latent heat flux, due to the El Niño effect, are much larger and the growth of SST errors is more notable, which yields the enhanced SPB for pIOD events with El Niño. Then, how does El Niño affect the variation in latent heat flux and finally cause the enhanced SPB?

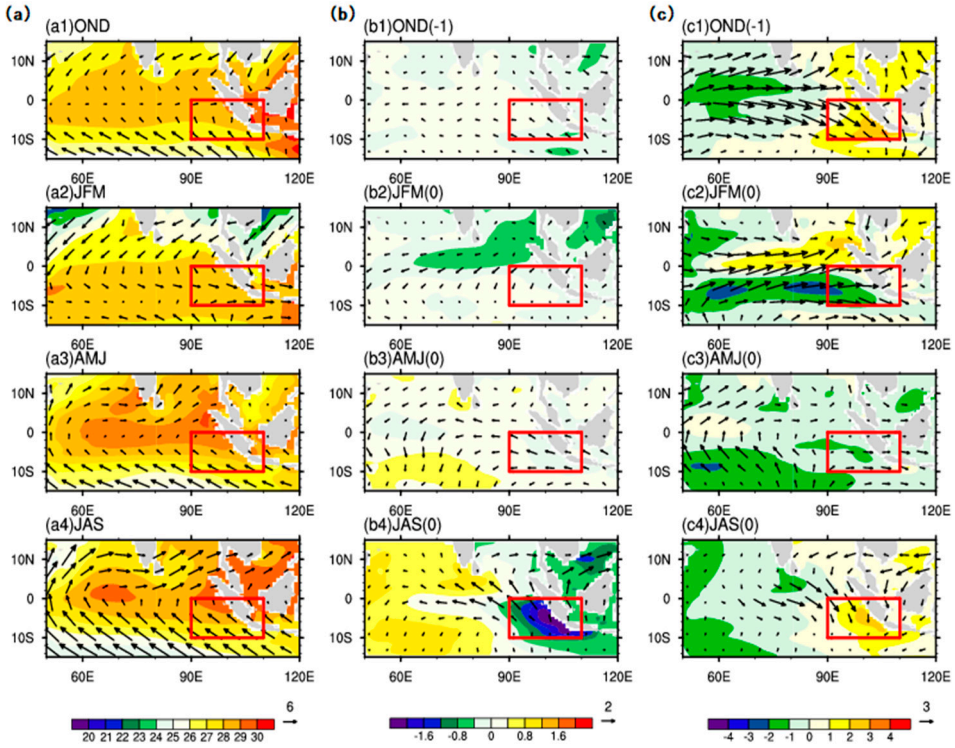

Figure 6. (**a**) Seasonal evolutions for the SST (shaded; units: °C) and surface wind (vectors; units: m/s) of climatological state in Indian Ocean. (**b**) Seasonal evolutions of SSTAs and related wind anomalies of the referenced five pIOD events that occurred with El Niño. (**c**) Seasonal evolutions of SST errors and wind anomalies generated by type-1 initial errors with start month being October (−1). The red rectangle represents the location of the southeastern IO.

4.2. Dynamic Mechanism Related to SPB Enhanced by El Niño

In present study, we found that SPB for pIOD predictions is enhanced by El Niño. The occurrence of SPB is due to the seasonal variation in latent heat flux in both IOD events accompanied by El Niño and pure IOD events, while the positive anomalies of latent heat flux for IOD events with El Niño (Figure 8) in summer are almost twice those for pure IOD events shown in Liu et al. [17], which indicates that the intensified seasonality of latent heat flux may be responsible for the enhanced SPB by El Niño. Since the variation in latent heat flux is closely related to the interaction between climatological wind and anomalous wind generated by initial errors and pIOD events, we paid attention to how El Niño affects such processes. As mentioned in the previous section, both types of initial errors tend to cause nIOD-like mode SST errors in IO, with positive values in SEIO and negative values in WIO. Thus, the seasonal growth rate of SST errors in WIO and SEIO induced by type-1 initial errors are compared in Figure 9. It is shown that the seasonal rate of increasing SST errors in SEIO is much stronger than that of WIO. Therefore, we focused only on how El Niño affects the seasonal variation in SST errors in SEIO in order to classify the enhanced SPB.

As mentioned earlier, the changes in latent heat flux are mainly brought about by the interaction between the wind anomalies caused by the initial errors, climatological wind and the anomalous wind of the pIOD event itself. The annual climatological wind presents a stable westerly component over the SEIO during autumn and winter, and the southeasterly during spring and summer with the strongest wind occurred in summer. The effects of El Niño on the variations in anomalous wind caused by initial errors and different IOD events should be noted.

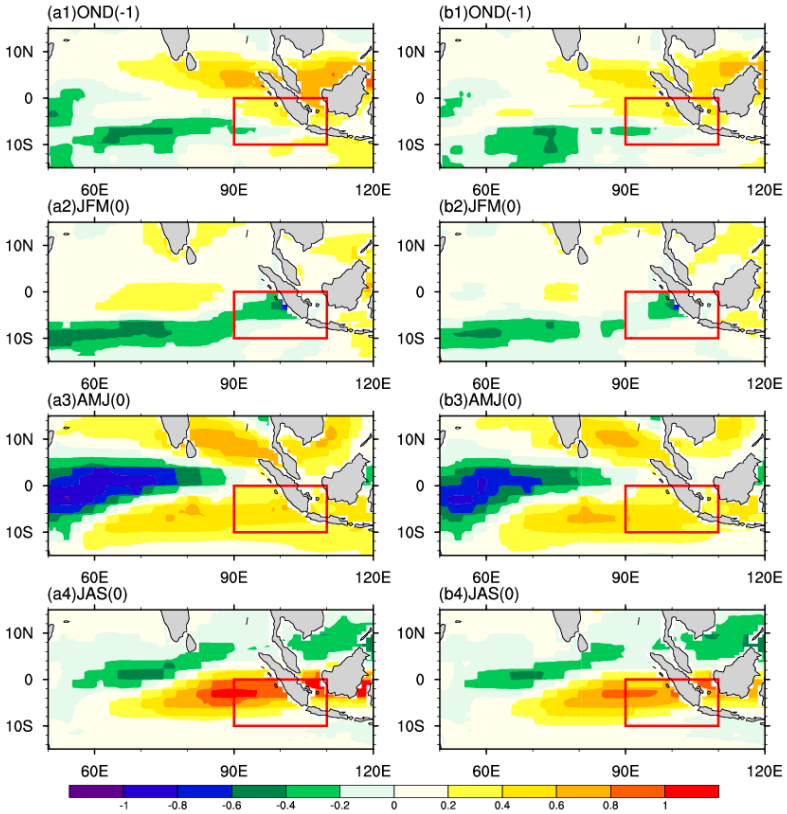

Figure 7. Seasonal variation in latent heat flux caused by (**a**) the type-1 and (**b**) the type-2 initial errors with the start month being October (−1). The inhibition of the loss of the latent heat flux is positive in the figures.

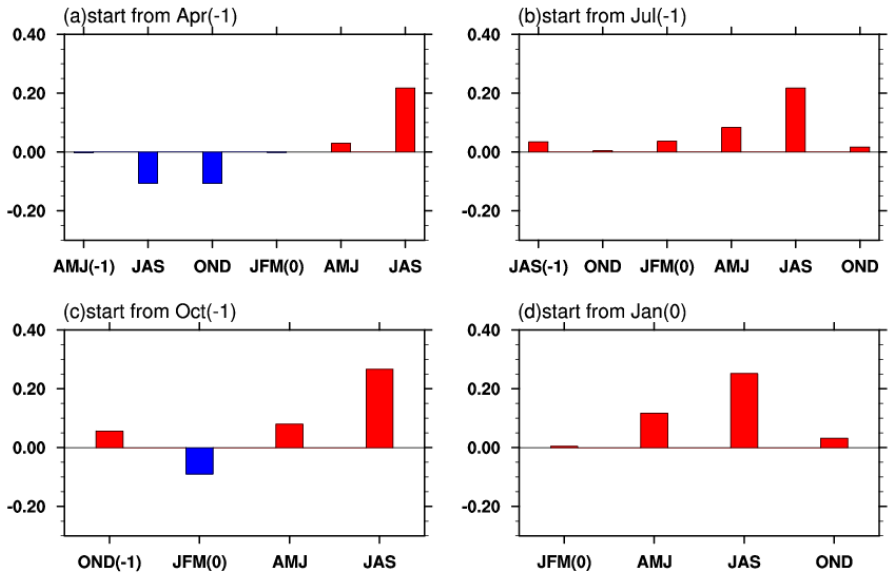

Figure 8. Seasonal mean of latent heat flux over the east pole of IOD with the start months being (**a**) April (−1), (**b**) July (−1), (**c**) October (−1) and (**d**) January (0).

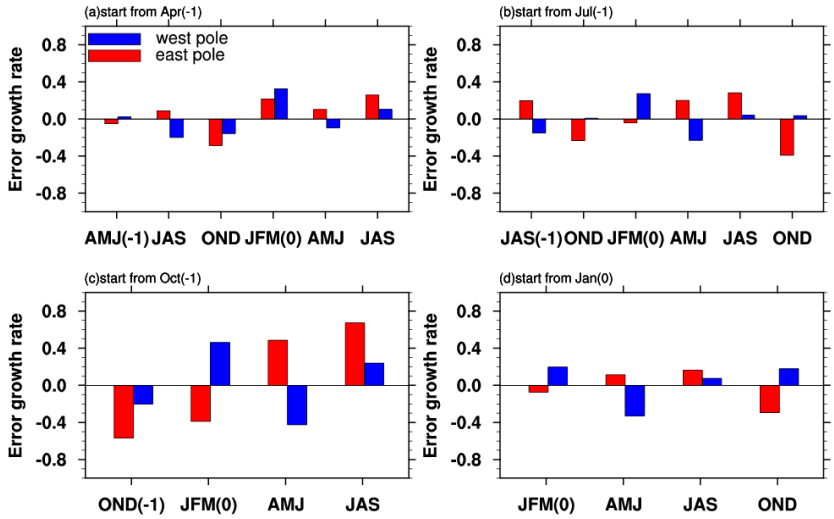

Figure 9. Ensemble mean of the growth rate for SST errors over the east and west poles induced by type-1 initial errors (histograms), with the start month being (**a**) April (−1), (**b**) July (−1), (**c**) October (−1) and (**d**) January (0).

Under the effects of El Niño, the distinct evolution of initial errors for IOD occurring with El Niño and pure IOD events (see [17]) results in differences in the strength and direction of wind anomalies over SEIO. Firstly, we compared the intensity of anomalous wind induced by initial errors between the pIOD events occurring with El Niño and the pure IOD events (Figure 10). For the four start months, the strength of wind anomalies for pIOD events occurring with El Niño in summer was larger than that of the pure IOD events, but weaker in spring. As the intensity of climatological wind over SEIO is stronger in summer than in the other three seasons, the initial errors induced by enhanced anomalous wind will be suppressed much more significantly by climatological wind in summer compared to other seasons. Therefore, the loss of latent heat flux is less in summer, which causes the positive SST errors to grow faster in summer and finally enhance the SPB for pIOD predictions. Moreover, beyond the magnitude of wind anomalies caused by initial errors, the direction of wind is another factor that will be responsible for the intensified seasonality of latent heat flux. For the pIOD events occurring with El Niño, the evolution of sea temperature errors over PO is similar to the decaying phase of La Niña; the sustained negative SST errors over the PO are favorable for the stable easterly anomalies. Through the effects of double-cell Walker circulation, there remains an anomalous westerly over the SEIO during the evolution of prediction errors. Such westerly anomalies appear much earlier than in pure IOD events, where they almost occur around spring (Figures 11 and 12). Climatological westerlies over SEIO during autumn and winter will stimulate the anomalous westerlies caused by initial errors and intensify the loss of latent heat flux, which is helpful for enhancing the seasonality of latent heat flux. Consequently, as the earlier appearance of westerly anomalies with its magnitude is much stronger in summer, which is greatly suppressed by climatological wind and pIOD-related anomalous wind, the loss of latent heat flux is limited in summer and stimulated in autumn and winter, and the seasonality of latent heat flux becomes more significant. Therefore, a stronger SPB for pIOD events occurring with El Niño arises.

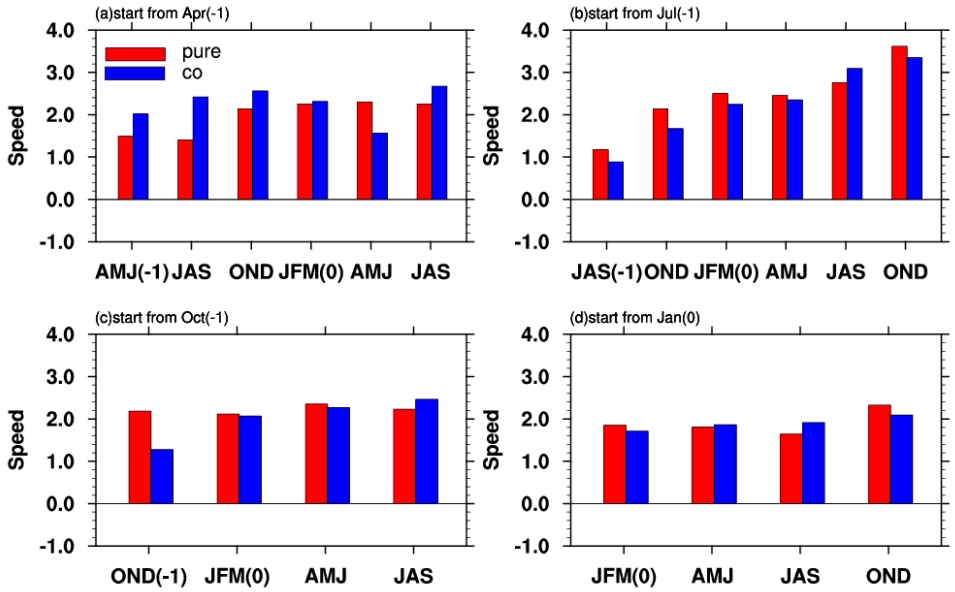

Figure 10. Histograms of the seasonal mean for wind strength produced by SPB-related initial errors for the pure IOD events and pIOD events that occurred with El Niño. Red bars represent the pure IOD events; blue bars represent the IOD predictions occurred with El Niño for (**a**) start month of April (−1), (**b**) start month of July (−1), (**c**) start month of October (−1) and (**d**) start month of January (0).

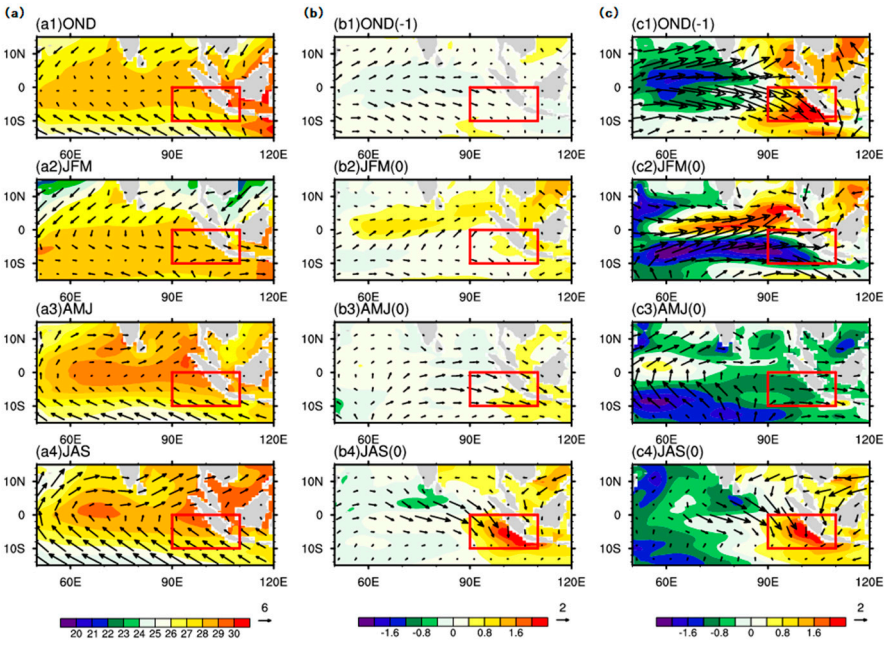

Figure 11. (**a**) Seasonal evolutions for the SST (shaded; units: °C) and surface wind (vectors; units: m/s) of climatological state in Indian Ocean. Seasonal evolutions of SST errors and wind anomalies induced by the type-1 initial errors for (**b**) the pure IOD events and (**c**) the pIOD events that occurred with El Niño with the start month being October (−1). The red rectangle denotes the location of the southeastern IO.

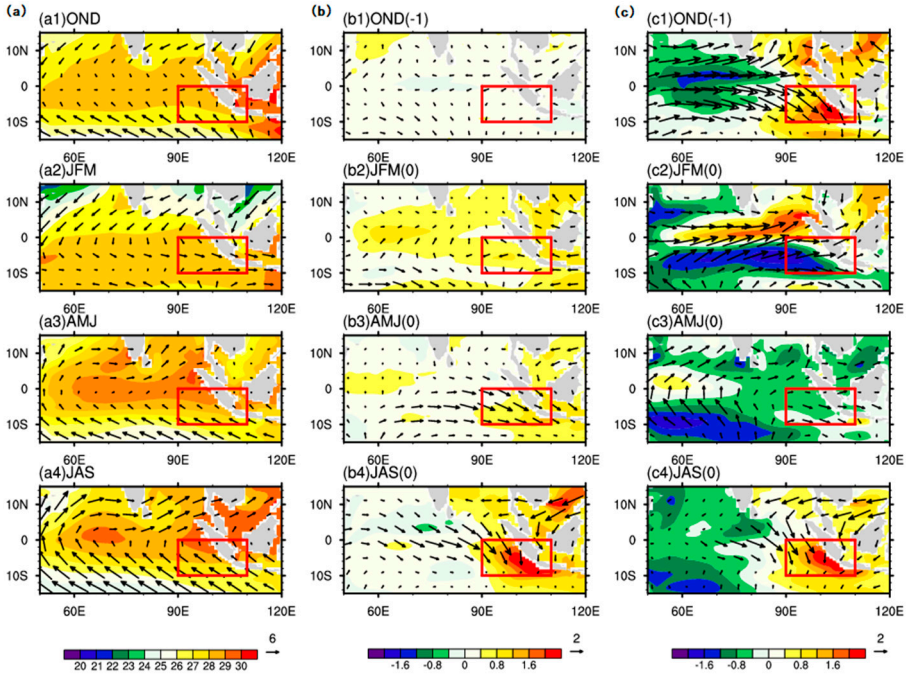

Figure 12. Same as Figure 11, (**a**) for the climatological state, but (**b**) for the pure IOD events and (**c**) for the pIOD events that occurred with El Niño induced by the type-2 initial errors.

Apart from the suppression of climatological wind on anomalous wind derived from initial errors, the IOD-related anomalous wind also plays an important role in the emergence of SPB, which implies that the different reference states are another factor that affects the strength of SPB. By comparing the development of SSTAs for pIOD events occurring with El Niño and pure IOD events (Figure 13), we found, under the effects of anomalous southeasterlies, that the negative SSTAs appear over SEIO in spring, and then the negative SSTAs develop along with the wind anomalies, which intensify for both types of IOD events. However, there exist some differences for SSTAs over WIO, with the positive SSTAs of the pIOD events occurring with El Niño being much larger than those of the pure IOD events, especially in summer. The zonal gradient of SSTAs over IO is greater for the pIOD events occurring with El Niño. As the IOD events are measured by the difference in SSTAs between SEIO and WIO, the larger the zonal gradient of SSTAs, the stronger the IOD events. When pIOD occurs with El Niño, the amplitude of IOD is intensified. Since IOD is an air–sea coupling phenomenon, the corresponding wind anomalies over SEIO are also stronger than during pure IOD events (Figure 14). The anomalous wind induced by stronger IOD occurring with El Niño would further restrict the westerly anomalies generated by initial errors; the loss of latent heat flux is reduced and finally the intensity of SPB is affected.

Under the effect of El Niño, the northwesterlies caused by initial errors appear earlier in SEIO and their strength is intensified in summer; meanwhile, the referenced IOD events are stronger compared to the pure IOD events, and the wind anomalies generated by initial errors are greatly suppressed in summer compared to other seasons; thus, the seasonality of latent heat flux is more remarkable. In particular, the loss of latent heat flux during summer decreases more significantly, which is more favorable for the development of positive SST errors and yields more prominent SPB.

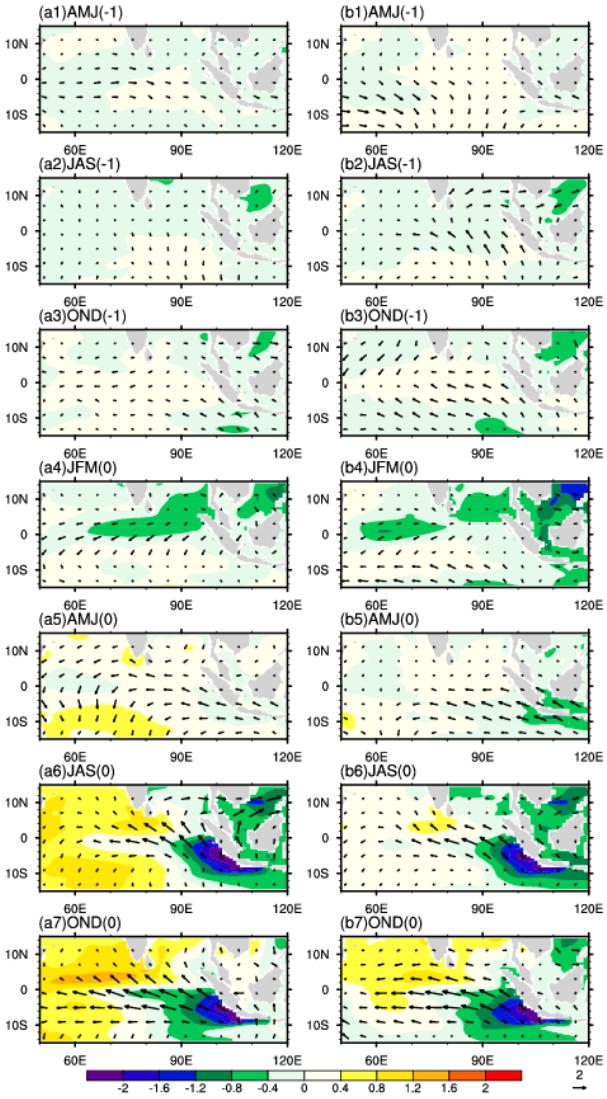

Figure 13. Seasonal evolutions of SSTAs (shaded; units: °C) and related surface wind anomalies (vectors; units: m/s) generated by (**a**) the five pIOD events that occurred with El Niño and (**b**) the five pure IOD events.

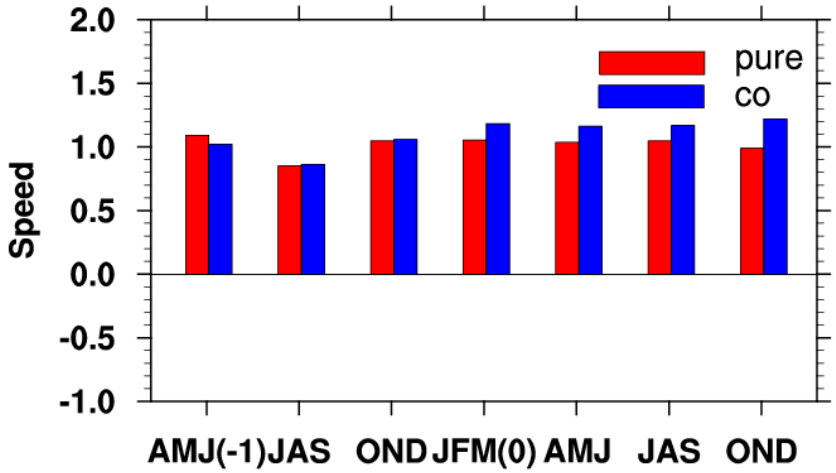

Figure 14. Histograms of the seasonal mean for wind strength produced by the pure IOD events and pIOD events that occurred with El Niño. Red bars represent the pure IOD events; blue bars represent the pIOD events that occurred with El Niño.

5. Summary and Discussion

In the present study, the Geophysical Fluid Dynamics Laboratory (GFDL) CM2p1 coupled model is used to investigate the effects of El Niño on the summer predictability barrier (SPB) of the Indian Ocean dipole (IOD), under the assumption that the prediction uncertainties are totally induced by the initial errors. We demonstrate that, under the influence of El Niño, the intensity of SPB tends to be stronger. Features of the initial errors that induce a significant SPB for the positive IOD (pIOD) events that occur with El Niño are exhibited, and there are two types of initial errors that tend to cause prediction errors to develop rapidly in summer. The first type is characterized by negative sea surface temperature (SST) errors over the central Pacific Ocean (PO) and negative subsurface sea temperature errors in the eastern PO. The SST errors in the Indian Ocean (IO) are negative, and the subsurface sea temperature errors present a dipole mode, with large positive values in the eastern IO. The other type of initial error shows a similar pattern to the first type, where negative SSTAs move eastward and are located in the eastern PO, while the spatial pattern of IO is opposite to the first type. By tracking the evolutions of the initial errors, it is shown that both types of initial errors present a La Niña-like decaying mode in the PO, which induces easterly anomalies in the PO. Through the gear effect of double-cell Walker circulation, anomalous westerlies occur in the eastern IO and lead to a negative IOD (nIOD) evolving mode, with positive SST errors occurring over the east pole (10° S-0°, 90° E-110° E) of the IOD, which dominate the season-dependent evolution of the prediction errors and cause the pIOD events to be underestimated. Even though the patterns in IO are quite different between these two types of initial errors, the prediction errors are mainly caused by the initial errors of the PO.

Under the effects of El Niño, the growth of prediction errors for pIOD occurring with El Niño is much faster in summer, which leads to an enhanced SPB, which is mainly caused by the stronger seasonal variation in latent heat flux, with the least loss appearing in summer. The enhanced seasonality of latent heat flux is modulated by the initial error-induced anomalous wind being greatly suppressed by climatological wind and the wind anomalies related to pIOD events. Considering the effects of El Niño, the northwesterlies over the southeastern IO are intensified in summer, which are greatly inhibited by climatological easterlies, and the loss of latent heat flux significantly decreases. Furthermore, when the pIOD events occur with El Niño, the westerly anomalies occur much earlier, and climatological westerlies that appear in autumn and winter will stimulate such anomalous wind and intensify the loss of latent heat flux. Thus, as the loss of latent heat flux is reinforced in autumn and winter and weakened in summer, the seasonality of latent heat flux becomes more prominent. Moreover, the amplitude of pIOD events occurring with El Niño is larger than that of the pure IOD events, which implies that anomalous wind related to the pIOD event itself will also affect the wind anomalies generated by initial errors more remarkably. Specifically, the anomalous westerlies caused by initial errors are prohibited more prominently by the stronger southeasterlies related to pIOD events during summer, which is beneficial for the appearance of a stronger SPB phenomenon. Therefore, El Niño could enhance the SPB for pIOD predictions by affecting the evolutions of initial errors and the strength of pIOD events, which leads to the westerlies caused by initial errors being prominently suppressed during summer and greatly decreases the loss of latent heat flux.

As mentioned in the Introduction, previous studies have shown that the effect of El Niño/Southern Oscillation (ENSO) on IOD predictability is complicated [19,31]. In this study, we further explored the variation in IOD predictability considering the influence of El Niño from the aspect of error growth, and found that the strength of the predictability barrier for pIOD events changed obviously, with SPB being intensified and WPB weakened. The enhanced SPB will result in the pIOD events being weakened and even becoming negative IOD (nIOD). Such results indicate that El Niño could modulate the prediction of the amplitude of pIOD events. This perspective coincides with the conclusions of Kug et al. [29] and Wang et al. [30], while the present study further revealed the initial error most likely to affect IOD predictability under the effect of ENSO. ENSO is an unignored

factor for IOD predictions, but its effect on IOD predictability could be used to guide improvements in the prediction of IOD.

As mentioned in the above section, when IOD occurs with ENSO, pIOD events are usually accompanied by El Niño and nIOD by La Niña [36]. As the strength of pIOD is stronger than nIOD, only the predictability of pIOD and the effects of El Niño were investigated in the present study. The nIOD is the symmetric opposite phase of pIOD as well as the relationship between El Niño and La Niña; how does La Niña affect the predictability of nIOD and are the effects opposite to the results in this study? Furthermore, considering the effects of La Niña, what are the main features of the initial errors? All these questions need to be addressed in further research.

According to the results shown in this study, as well as Liu et al. [17], particular spatial patterns of initial errors are crucial components in the emergence of the predictability barrier for IOD events. Moreover, the anomalies of the initial errors that yield large prediction errors are usually concentrated in a few regions. This implies that increasing the observations in these regions and assimilating them into the model may significantly decrease the SPB and associated prediction errors for IOD, and the prediction skills of IOD could be greatly improved. This argument is associated with the concept of "target observation" [42]. Obviously, the results mentioned in this study could provide valid information for determining the target observations for IOD predictions. Undoubtedly, further research needs to be conducted to verify whether the regions associated with initial errors represent the optimal locations for target observations or not.

Author Contributions: All the authors have contributed to this research. Conceptualization, W.D.; data curation, D.L.; methodology, W.D.; visualization, D.L.; writing—original draft, D.L.; writing—review & editing, W.D. and R.F. All authors have read and agreed to the published version of the manuscript.

Funding: This work was jointly supported by the National Natural Science Foundation of China (Grant Nos. 41930971 & 41525017) and the Open Research Program at the State Key Laboratory of Atmospheric Sciences and Geophysical Fluid Dynamics.

Institutional Review Board Statement: Not applicable.

Informed Consent Statement: Not applicable.

Data Availability Statement: The data presented in this study will be available to the researchers upon request.

Acknowledgments: The authors are very grateful for the useful comments provided by the three anonymous reviewers. This work was jointly supported by the National Natural Science Foundation of China (Grant Nos. 41930971 & 41525017) and the Open Research Program at the State Key Laboratory of Atmospheric Sciences and Geophysical Fluid Dynamics.

Conflicts of Interest: The authors declare no conflict of interest.

References

1. Saji, N.H.; Goswami, B.N.; Vinayachandran, P.N.; Yamagata, T. A dipole mode in the tropical Indian Ocean. *Nature* **1999**, *401*, 360–363. [CrossRef]
2. Webster, P.J.; Moore, A.M.; Loschnigg, J.P.; Leben, R.R. Coupled ocean–atmosphere dynamics in the Indian Ocean during 1997–1998. *Nature* **1999**, *401*, 356–360. [CrossRef]
3. Saji, N.H.; Yamagata, T. Structure of SST and surface wind variability during Indian Ocean dipole mode events: COADS observations. *J. Clim.* **2003**, *16*, 2735–2751. [CrossRef]
4. Murtugudde, R.; McCreary, J.P.; Busalacchi, A.J. Oceanic processes associated with anomalous events in the Indian Ocean with relevance to 1997–1998. *J. Geophys. Res. Ocean.* **2000**, *105*, 3295–3306. [CrossRef]
5. Song, Q.; Vecchi, G.A.; Rosati, A.J. Indian Ocean variability in the GFDL coupled climate model. *J. Clim.* **2007**, *20*, 2895–2916. [CrossRef]
6. Annamalai, H.; Murtugudde, R. Role of the Indian Ocean in regional climate variability. *Earth's Clim. Ocean Atmos. Interact.* **2004**, *147*, 213–246.
7. Ansell, T.; Reason, C.J.C.; Meyers, G. Variability in the tropical southeast Indian Ocean and links with southeast Australian winter rainfall. *Geophys. Res. Lett.* **2000**, *27*, 3977–3980. [CrossRef]

8. Ashok, K.; Guan, Z.; Yamagata, T. Impact of the Indian Ocean dipole on the relationship between the Indian monsoon rainfall and ENSO. *Geophys. Res. Lett.* **2001**, *28*, 4499–4502. [CrossRef]
9. Black, E.; Slingo, J.; Sperber, K.R. An observational study of the relationship between excessively strong short rains in coastal East Africa and Indian Ocean SST. *Mon. Weather Rev.* **2003**, *131*, 74–94. [CrossRef]
10. Birkett, C.; Murtugudde, R.; Allan, T. Indian Ocean climate event brings floods to East Africa's lakes and the Sudd Marsh. *Geophys. Res. Lett.* **1999**, *26*, 1031–1034. [CrossRef]
11. Clark, C.O.; Webster, P.J.; Cole, J.E. Interdecadal variability of the relationship between the Indian Ocean zonal mode and East African coastal rainfall anomalies. *J. Clim.* **2003**, *16*, 548–554. [CrossRef]
12. Saji, N.H.; Yamagata, T. Possible impacts of Indian Ocean dipole mode events on global climate. *Clim. Res.* **2003**, *25*, 151–169. [CrossRef]
13. Dommenget, D.; Jansen, M. Predictions of Indian Ocean SST indices with a simple statistical model: A null hypothesis. *J. Clim.* **2009**, *22*, 4930–4938. [CrossRef]
14. Landman, W.A.; Mason, S.J. Forecasts of Near-Global Sea Surface Temperatures Using Canonical Correlation Analysis. *J. Clim.* **2001**, *14*, 3819–3833. [CrossRef]
15. Luo, J.J.; Masson, S.; Behera, S.; Yamagata, T. Experimental forecasts of the Indian Ocean dipole using a coupled OAGCM. *J. Clim.* **2007**, *20*, 2178–2190. [CrossRef]
16. Shi, L.; Hendon, H.H.; Alves, O.; Luo, J.J.; Balmaseda, M.; Anderson, D. How predictable is the Indian Ocean dipole? *Mon. Weather Rev.* **2012**, *140*, 3867–3884. [CrossRef]
17. Liu, D.; Duan, W.; Feng, R.; Tang, Y. Summer Predictability Barrier of Indian Ocean Dipole Events and Corresponding Error Growth Dynamics. *J. Geophys. Res. Ocean.* **2018**, *123*, 3635–3650. [CrossRef]
18. Liu, H.; Tang, Y.; Chen, D.; Lian, T. Predictability of the Indian Ocean Dipole in the coupled models. *Clim. Dyn.* **2016**, *48*, 1–20. [CrossRef]
19. Feng, R.; Duan, W.S. The spatial patterns of initial errors related to the "winter predictability barrier" of the Indian Ocean dipole. *Atmos. Ocean. Sci. Lett.* **2015**, *7*, 406–410.
20. Li, T.; Wang, B.; Chang, C.P.; Zhang, Y. A theory for the Indian Ocean dipole–zonal mode. *J. Atmos. Sci.* **2003**, *60*, 2119–2135. [CrossRef]
21. Stuecker, M.F.; Timmermann, A.; Jin, F.F.; Chikamoto, Y.; Zhang, W.; Wittenberg, A.T.; Zhao, S. Revisiting ENSO/Indian Ocean Dipole phase relationships. *Geophys. Res. Lett.* **2017**, *44*, 2481–2492. [CrossRef]
22. Alexander, M.A.; Bladé, I.; Newman, M.; Lanzante, J.R.; Lau, N.C.; Scott, J.D. The atmospheric bridge: The influence of ENSO teleconnections on air–sea interaction over the global oceans. *J. Clim.* **2002**, *15*, 2205–2231. [CrossRef]
23. Chen, D. Indo-Pacific Tripole: An intrinsic mode of tropical climate variability. *Adv. Geosci.* **2011**, *24*, 1–18.
24. Zhang, Y.; Du, Y.; Zheng, S.; Yang, Y.; Cheng, X. Impact of Indian Ocean Dipole on the salinity budget in the equatorial Indian Ocean. *J. Geophys. Res. Ocean.* **2013**, *118*, 4911–4923.
25. Yuan, D.; Zhou, H.; Zhao, X. Interannual climate variability over the tropical Pacific Ocean induced by the Indian Ocean dipole through the Indonesian Throughflow. *J. Clim.* **2013**, *26*, 2845–2861. [CrossRef]
26. Yuan, D.; Hu, X.; Xu, P.; Zhao, X.; Masumoto, Y.; Han, W. The IOD-ENSO precursory teleconnection over the tropical Indo-Pacific Ocean: Dynamics and long-term trends under global warming. *J. Oceanol. Limnol.* **2018**, *36*, 4–19. [CrossRef]
27. Wang, X.; Wang, C. Different impacts of various El Niño events on the Indian Ocean Dipole. *Clim. Dyn.* **2015**, *42*, 991–1005. [CrossRef]
28. Zhu, J.; Huang, B.; Kumar, A.; Kinter, J.L. Seasonality in Prediction Skill and Predictable Pattern of Tropical Indian Ocean SST. *J. Clim.* **2015**, *28*, 801–809. [CrossRef]
29. Kug, J.S.; Kang, I.S.; Lee, J.Y.; Jhun, J.G. A statistical approach to Indian Ocean sea surface temperature prediction using a dynamical ENSO prediction. *Geophys. Res. Lett.* **2004**, *31*, 399–420. [CrossRef]
30. Wang, L.W.; Zheng, F.; Zhu, J. Preliminary Studies on Predicting the Tropical Indian Ocean Sea Surface Temperature through Combined Statistical Methods and Dynamic ENSO Prediction. *Atmos. Ocean. Sci. Lett.* **2013**, *6*, 52–59.
31. Ding, R.; Li, J. Influences of ENSO teleconnection on the persistence of sea surface temperature in the tropical Indian Ocean. *J. Clim.* **2012**, *25*, 8177–8195. [CrossRef]
32. Carton, J.A.; Grodsky, S.A.; Liu, H. Variability of the oceanic mixed layer, 1960–2004. *J. Clim.* **2008**, *21*, 1029–1047. [CrossRef]
33. Delworth, T.L.; Broccoli, A.J.; Rosati, A.; Stouffer, R.J.; Balaji, V.; Beesley, J.A.; Durachta, J.W. GFDL's CM2 global coupled climate models. Part I: Formulation and simulation characteristics. *J. Clim.* **2006**, *19*, 643–674. [CrossRef]
34. Griffies, S.M. Elements of MOM4p1: GFDL Ocean Group Tech. Rep. 6. NOAA. Geophysical Fluid Dynamics Laboratory; 2009. Available online: https://www.gfdl.noaa.gov/wp-content/uploads/files/model_development/ocean/guide4p1.pdf (accessed on 23 October 2021).
35. Cai, W.; Rensch, P.V.; Cowan, T.; Hendon, H.H. An Asymmetry in the IOD and ENSO Teleconnection Pathway and Its Impact on Australian Climate. *J. Clim.* **2012**, *25*, 6318–6329. [CrossRef]
36. Zhang, W.; Wang, Y.; Jin, F.F.; Stuecker, M.F.; Turner, A.G. Impact of different El Niño types on the El Niño/IOD relationship. *Geophys. Res. Lett.* **2016**, *42*, 8570–8576. [CrossRef]
37. McPhaden, M.J. Tropical Pacific Ocean heat content variations and ENSO persistence barriers. *Geophys. Res. Lett.* **2003**, *30*, 319–338. [CrossRef]

38. Duan, W.; Liu, X.; Zhu, K.; Mu, M. Exploring the initial errors that cause a significant "spring predictability barrier" for El Niño events. *J. Geophys. Res. Ocean.* **2009**, *114*, C04022. [CrossRef]
39. Wajsowicz, R.C. Potential predictability of tropical Indian Ocean SST anomalies. *Geophys. Res. Lett.* **2005**, *32*, L24702. [CrossRef]
40. Du, Y.; Xie, S.P.; Huang, G.; Hu, K. Role of air-sea interaction in the long persistence of El Nino-induced north Indian Ocean warming. *J. Clim.* **2009**, *22*, 2023–2038. [CrossRef]
41. Chakravorty, S.; Chowdary, J.S.; Gnanaseelan, C. Spring asymmetric mode in the tropical Indian Ocean: Role of El Nino and IOD. *Clim. Dyn.* **2013**, *40*, 1467–1481. [CrossRef]
42. Synder, C. Summary of an informal workshop on adaptive observations and FASTEX. *Bull. Amer. Meteor. Soc.* **1996**, *77*, 953–961. [CrossRef]